Microscopic evidences for intercalation of nickel and iron into layered oxysulfide La2O2S2

Shunsuke Sasaki, Dalel Driss, Maria Teresa Caldes, Eric Gautron, Sylvian Cadars, Etienne Janod, Benoit Corraze, Catherine Guillot-Deudon, Isabelle Braems, Stéphane Jobic, et al.

Microscopic evidences for intercalation of nickel and iron into layered oxysulfide $La_2O_2S_2$

Shunsuke Sasaki[*a], Dalel Driss[a], Maria Teresa Caldes[a], Eric Gautron [a], Sylvian Cadars[b], Etienne Janod[a], Benoit Corraze[a], Catherine Guillot-Deudon[a], Isabelle Braems[a], Stéphane Jobic[*a], and Laurent Cario[*a]

[a] Nantes Université, CNRS, Institut des Matériaux de Nantes Jean Rouxel, IMN, F-44000 Nantes, France

[b] Université de Limoges, CNRS, Institut de recherche sur les céramiques, IRCER, 12 rue Atlantis, 87068 Limoges, France

Keywords: Low-dimensional materials, oxychalcogenides, intercalation, anion redox

ABSTRACT: 2D transition metal chalcogenides have been examined as versatile platforms for exotic quantum phenomena, optoelectronic and photocatalytic applications. $La_2O_2S_2$, a layered oxysulfide built of $[La_2O_2]^{2+}$ slabs and 2D arrays of $[S_2]^{2-}$ dimers, was recently found to be a promising precursor to fabricate such 2D materials. Redox reactions with external zerovalent metals cleaved its S-S bonds, triggering intercalation of those metal guests. This process serves as a novel approach to construct 2D metal sulfides between rigid $[La_2O_2]^{2+}$ slabs, but so far demonstrated only for Cu^+ cations. We herein report that the same intercalation process takes place also when Ni and Fe were used as reagents. While XRD indicated that the reactions with Ni and Fe converted $La_2O_2S_2$ into the sulfur-deficient $La_2O_2S_{1.5-x}$ ($0 \leq x \leq 0.38$) phase, our TEM analyses evidenced diffusion of those metals in between $[La_2O_2]^{2+}$ slabs at the local scale. This finding suggested the formation of 2D nickel and iron sulfides intergrown with $[La_2O_2]^{2+}$ slabs, either as the unprecedented La-O-M-S (M = Ni, Fe) phase, or a biphasic heterostructure. In addition, our computational structure prediction also supported stability of such intergrowth $[La_2O_2][M_xS_{2-y}]$ structures, encouraging future attempts to isolate those elusive 2D materials.

1. Introduction

Low-dimensional compounds belong to a specific family of materials characterized by a strong anisotropy in the chemical bonding, and consequently in electronic, magnetic and thermal properties. 2D transition metal dichalcogenides (TMDCs) likely represent one of their most famous members. TiS_2 is the well-known cathode material that Whittingham and co-workers used for fabricating the very first archetypical Li-ion battery[1]. In addition, most TDMCs have been subject to long-standing researches on superconductivity[2-4], charge-density and spin-density waves[5-7], quantum spin hall effects[8] as well as more emerging applications like electro- or photo-catalysis[9] and neuromorphic devices[10]. Such exotic properties are not limited to TMDCs: intrinsic ferromagnetic topological state in $MnBi_8Te_{13}$[11], and high-T_c superconductivity emerging from nematic order in FeSe[12] are likely the most recent and striking examples that brought about breakthrough in fundamental physics and future electronics of materials with a marked 2D structure.

Accordingly, explorations of novel 2D metal chalcogenides have been a long-standing challenge for solid-state chemists. One approach was post-synthetic modification of layered precursors by means of (de)intercalation. Some seminal examples are oxidative deintercalation of alkali metals from $LiVS_2$[13] and $KCrSe_2$[14] using I_2 in acetonitrile, which respectively led to metastable 2D CdI_2-type VS_2 and $CrSe_2$. The similar oxidative deintercalation was applied more recently to prepare 2D V_2Ch_2O (Ch = Se, Te) from their Cs and Rb quaternary precursors[15-16]. Equally, Rodriguez and co-workers have succeeded in preparing 2D FeS superconductor and its CoCh (Ch = S, Se) analogs by hydrothermal deintercalation K^+ from $K_{1-x}Fe_{2-y}S_2$ and $K_{1-x}Co_2Ch_2$, respectively[17-18].

These pre-existing strategies are based on the removal (the insertion) of a cation from (into) a van der Waals (vdW) gap between pre-formed 2D metal chalcogenide slabs with oxidation (reduction) of a metal and change of its d electron counting. The present study also employs a post-synthetic route, but it instead constructs 2D metal chalcogenides by intercalation of metal cations in between host cationic layers with (partial or complete) reduction of the anion. Namely, sulfur dimers embedded in a lamellar precursor may undergo redox reactions with zerovalent metal intercalants M^0, triggering their S-S bond cleavage and their re-assembly around the guest cation M into novel MS_2 layers without a severe rearrangement of the overall structural edifice (Fig. 1). This new topochemical concept was demonstrated for the intercalation of Cu^+ into $La_2O_2S_2$, $Ba_2F_2S_2$ and $LaSe_2$ to form $La_2O_2Cu_2S_2$, $Ba_2F_2Cu_2S_2$ and $LaCuSe_2$, respectively [19-20]. While these products were already reported in the literature and prepared at high temperature, the reverse reaction (i.e. deintercalation of Cu^+), which was first demonstrated on $La_2O_2Cu_2S_2$ [19], paved the way to the discoveries of novel

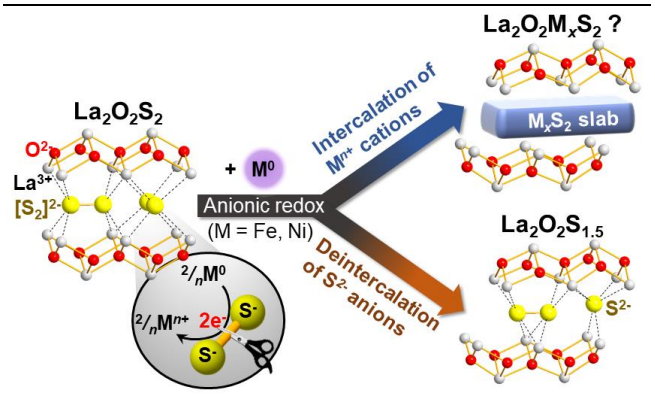

Fig. 1. The conceptual scheme describing topochemistry of layered oxysulfide $La_2O_2S_2$. The above process depicts in-situ 2D M_xS_2 layer construction by redox-initiated intercalation of metal intercalants. Its competing process leading to deintercalation of sulfur anions is displayed in the bottom part.

metastable polychalcogenides $Sr_2MnO_2Ch_2$[21] and $Bi_2O_2Ch_2$[22] (Ch= S, Se) from layered copper chalcogenides $Sr_2MnO_2Cu_{1.5}Ch_2$ and $Bi_2O_2Cu_2Ch_2$, respectively. Similarly, low-temperature reactions with Ni and Fe elements converted BaS_2 and BaS_3 into the respective low-dimensional sulfides $BaNiS_2$ and $BaFe_2S_3$, materials that could also be prepared at high temperature[23]. To explore novel 2D metal sulfides with possible interesting properties or functionalities, we herein examine the redox reactivity of $La_2O_2S_2$ with $[S_2]^{2-}$ dimers towards Fe^0 and Ni^0, in the quest of unprecedented La-O-M-S quaternary phases with a metastable lamellar structure. At the macroscopic scale, our X-ray diffraction analyses of the bulk revealed that the reaction with those transition metals conducts to the partial de-intercalation of sulfur species[24] from $La_2O_2S_2$, i.e. $La_2O_2S_{1.5-x}$ ($0 \leq x \leq 0.38$) (Fig. 1 bottom). Moreover, nanoscopic observation by scanning transmission electron microscopy (STEM) clearly evidenced that Ni and Fe cations diffused also in between $[La_2O_2]^{2+}$ slabs to interact with $[S_2]$ species, forming at the end a composite material built on the intergrowth of $La_2O_2S_{1.5-x}$ ($0 \leq x \leq 0.38$) and $[La_2O_2M_xS_2]$ (e.g. $x = 0.5$ or 1) blocks. This preliminary result is encouraging for future attempts to isolate new 2D transition metal compounds and to examine their potential functionalities and properties.

2. Experimental procedure

2.1. Syntheses

The precursor $La_2O_2S_2$ was prepared from La_2O_3, La_2S_3 and elemental sulfur at high temperature (T = 700 °C) following the method described previously[19]. To examine its reactivity towards Ni^0 metal, the yellow powder of $La_2O_2S_2$ was ground on an agate mortar with 0.5-2.0 molar equiv. of Ni powder (Aldrich, < 100 nm in average size, ≥ 99%). Then, the mixture was pelletized and sealed in an evacuated (~ 10^3 torr) silica tube. The sealed mixture was heated to 350 °C at a rate of 300 °C h^{-1}, held at this temperature for 2 h, and cooled to room temperature by turning-off the furnace. The obtained black pellet was thoroughly ground and stored under inert atmosphere before further characterization. The similar protocol was applied to the reaction with Fe^0 powder (Aldrich, 35-45 nm in average size, 99.5%). For Co^0, metallic Co nanoparticles were first prepared following the method reported by Zhao et al.[25] (< 1 µm in average size, > 99% trace metal basis as confirmed by SEM/EDX), and the Co^0-$La_2O_2S_2$ pellet was heated at 200°C.

The reaction with zerovalent Ni^0 specie was examined also in solvothermal condition. $La_2O_2S_2$ (ca. 150 mg), 1.0-2.0 equiv of $Ni(PPh_3)_2(CO)_2$ (Alfa Aesar, 98%) and anhydrous acetonitrile (~10 ml) were loaded into a PTFE autoclave (TOP Industrie, 20 ml volume) under inert atmosphere. Then, the autoclave was assembled and heated in an oven at 200 °C for 12-72 h before being cooled down to ambient temperature by turning-off the oven. Unreacted $Ni(PPh_3)_2(CO)_2$ forms a brittle colorless solid and could be separated easily from the black precipitate of the reaction mixture. The obtained black powder was washed with ethanol, toluene and acetone before drying under vacuum.

2.2. Structural and chemical characterizations

X-ray diffraction (XRD) patterns of all powder samples were recorded at room temperature on a Bruker D8 Advance diffractometer (Brag-Brentano geometry, θ-2θ) equipped with Cu Kα1 radiation (λ = 1.5406 Å), Ge (111) monochromator and LynxEye detector. The obtained diffraction patterns were analyzed by Rietveld refinement using on the TOPAS-Academic package (version 7). When needed, anisotropic microstrain was taken into account employing the Stephens tensor method[26]. Bulk compositions of the reaction mixtures were inspected by energy-dipersive X-ray (EDX) spectroscopy on a JEOL 5800LV scanning electron microscope operating at 15 keV. The flat-polished specimens were prepared by impregnating the powder samples into an epoxy resin and subsequent grinding with ethanol/diamond grit suspensions. Scanning transmission electron microscopy (STEM) imagining was performed on a Cs-probe corrected STEM Themis Z G3 (Thermo Fisher Scientific) equipped with a high angle annular dark field (HAADF) detector operating at 80 or 300 kV accelerating voltage. EDX mapping was recorded by 4-SDD detectors Super-X system built in STEM apparatus.

2.3. Magnetometry and transport measurements

Magnetic properties were evaluated on a Quantum Design MPMS-XL7. The powder samples (*ca*. 100 mg) were wrapped in a plastic film and loaded into a plastic sample holder, whose diamagnetic signals were subtracted from magnetization data before further analyses. Firstly, direct current (DC) magnetization M versus magnetic field isotherm ($0 \leq H \leq 45$ kOe) was recorded at 300, 200, 100, 50, 10 and 2 K. DC magnetization was also measured as a function of temperature after zero-field cooling (ZFC); the temperature was swept from 2 K to 300 K under the applied filed H = 30 kOe.

Electric transport measurements were carried out for the sample from the solvothermal reaction with Ni^0 complex. Its powder sample was pressed into a pellet and annealed for 12 h at 200 °C in acetonitrile, which did not lead to any change on its XRD pattern (*Note: annealing under vacuum or inert atmosphere led to partial decomposition into hP-La_2O_2S*). The annealed pellet sample was attached to four gold wire electrodes using silver paste. The resistivity was evaluated by four-point method sweeping temperature between 300 and 2 K.

2.4 Computational structure prediction (CSP)

In this study, CSP of the La-O-Ni-S quaternary phase was carried out by employing the evolutionary algorithm package USPEX (Universal Structure Predictor: Evolutionary Xtallography)[27]. The CSP algorithm firstly generated 40 random structures complying composition and number of atoms per cell given in the input files. As a hypothesis, three compositions were supposed taking possible sulfur off-stoichiometry and different nickel uptakes into account: $La_2O_2NiS_2$ (Z = 2, 14 atoms), $La_2O_2Ni_{0.5}S_{1.5}$ (Z = 4, 24 atoms) and $La_2O_2Ni_{0.5}S_2$ (Z = 4, 26 atoms). Those randomly generated structures were subject to structure relaxation and total energy calculation at GGA-PBE functional of DFT-B3 method[28] with Becke-Johnson (BJ) damping[29] implemented in the VASP code. 70% of the lowest energy structures were used for producing a next generation; the 8 lowest-energy structures among them were retained without modification while the rest underwent heredity (40%), soft mutation (15%), atom permutation (15%), lattice mutation (10%) and symmetric random (20%) operations, which were defined in USPEX code. Iterations of the evolutionary algorithm were continued until the last 25 generations gave the same lowest-energy structures.

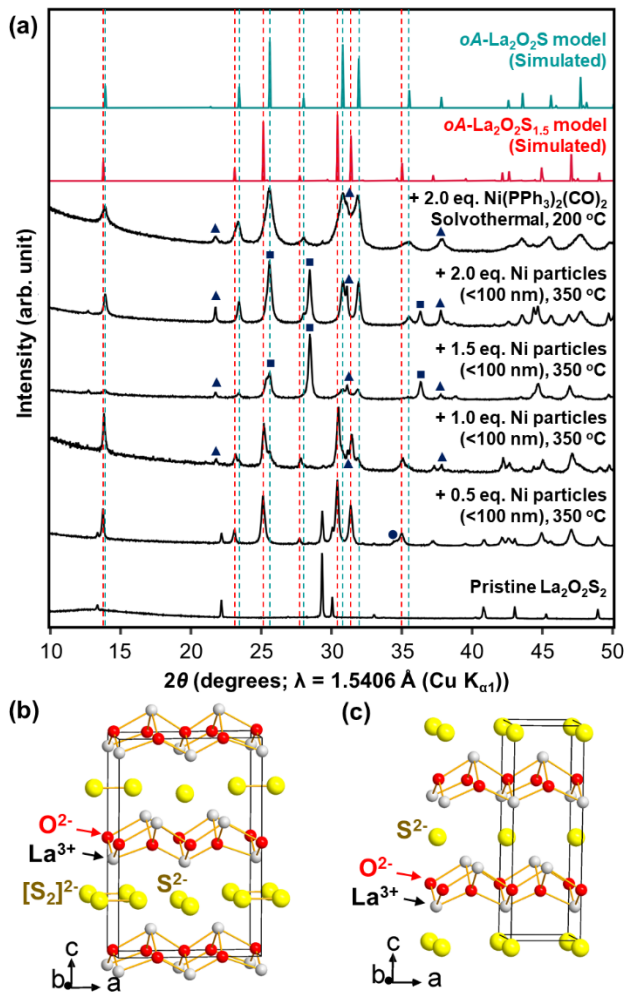

Fig. 2. (a) Structures of *oA*-$La_2O_2S_{1.5}$ and (b) *oA*-La_2O_2S (Space group *Amm*2) redrawn from the crystallographic data reported in ref 24. (c) Their simulated XRD pattern (red and cyan) compared to the experimental XRD (black) of the powder samples obtained from the reactions of $La_2O_2S_2$ with Ni^0 species in solid-solid or solvothermal conditions. Each symbol represents diffraction peaks from ■ = *hP*-La_2O_2S, ● = α-NiS and ▲ = Ni_3S_2, respectively. Pearson symbols (i.e. *oA*- and *hP*-) are used hereafter to discern polymorphs with a different symmetry

3. Results and discussion

3.1. Reactivity of $La_2O_2S_2$ towards Ni^0 metals

Figure 2a shows the X-Ray powder patterns obtained for the solid-solid reactions of $La_2O_2S_2$ with different amounts of Nickel metal. As previously reported, the reaction with 0.5 equiv. of Ni^0 powder leads to the metastable phase *oA*-$La_2O_2S_{1.5}$ with the *Amm*2 space group[24] (Fig. 2b) and cell parameters identical to those reported in the literature (Table S1).Throughout the process, the structural integrity of the quasi-quadratic, PbO-type $[La_2O_2]^{2+}$ slabs is retained but one-fourth of sulfur anions were removed from the system; i.e. half of the $(S_2)^{2-}$ dimers are substituted by S^{2-} anions. This partial deintercalation goes along with the formation of α-NiS with NiAs structure [30] (Fig. 2a) suggesting a reaction formulated as:

$$La_2O_2S_2 + 0.5\ Ni^0 \rightarrow La_2O_2S_{1.5} + 0.5\ NiS$$

However the XRD pattern of the "$La_2O_2S_2$+0.5Ni" product in Fig. 2a indicated the incomplete conversion of $La_2O_2S_2$. Actually, 0.5 equiv. of Ni^0 powder, could not complete the reaction even by extending reaction time (2 h → 72 h) or raising the reaction temperature (350 → 450 °C).

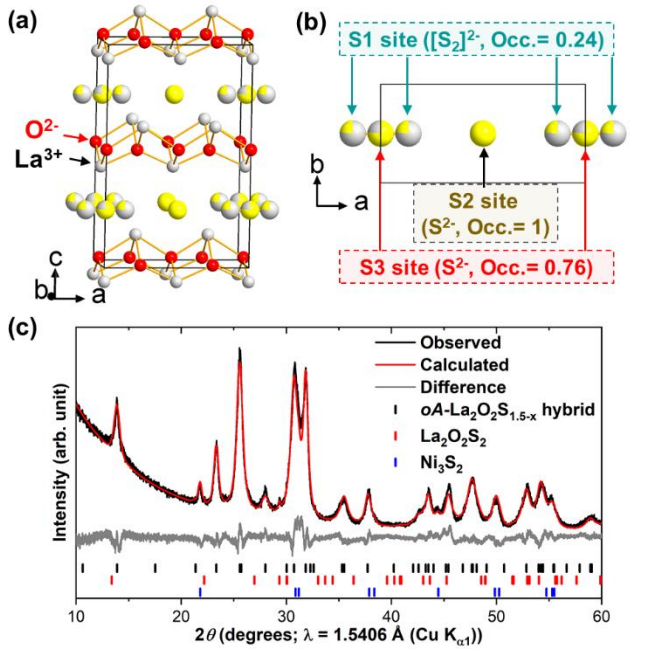

Fig. 3. (a) The "hybrid" structure model to represent *oA*-$La_2O_2S_{1.5-x}$ solid solution. (b) In-plane view showing the sulfur sites and their refined occupancies (Occ.). (c) Rietveld fit of PXRD pattern obtained from the reaction of $La_2O_2S_2$ with 2.0 $Ni(PPh_3)_2(CO)_2$ using the hybrid model. See Table S1 for details.

In contrast, increasing Ni^0 feeds (1.0-2.0 equiv.) could consume all the $La_2O_2S_2$ precursor (Fig. 2a). However Ni^0 feeds larger than 1.5 equiv. led to the formation as a side product of *hP*-La_2O_2S, the non-topochemical product where the quasi-quadratic $[La_2O_2]^{2+}$ slabs of $La_2O_2S_2$ was deformed into the hexagonal structure with *P*-3*m*1 space group[31]. To complete consumption of $La_2O_2S_2$ without decomposition into *hP*-La_2O_2S, the reactivity towards Ni^0 specie was examined also under solvothermal condition. Ni intercalation in solution state was recently demonstrated by Koski and co-workers employing disproportionation of Ni^{2+} salts with hydrazine at ambient temperature[32], or using thermal decomposition of triphenylphosphines (PPh_3) or cyclooctadiene (COD) complexes of zerovalent Ni^0 under acetone reflux (T = 56 °C)[33]. In our case, both metal intercalation and deintercalation of chalcogen anions required an elevated temperature at least above 200 °C[20,24], at which all those Ni sources would decompose or precipitate into Ni metal before reacting with the oxysulfides. Therefore, we herein decided to employ the zerovalent metal complex $Ni(PPh_3)_2(CO)_2$ as reducing agent. *In contrast to its non-substituted analog $Ni(CO)_4$ that is notorious for its toxicity, its volatility and its heat/light sensitivity*[34], $Ni(PPh_3)_2(CO)_2$ remains stable and non-volatile even at elevated temperature[35], and thus can be handled more safely.

The XRD pattern in Fig. 2a indicated that the solvothermal reaction with 2.0 equiv. of $Ni(PPh_3)_2(CO)_2$ completely converted $La_2O_2S_2$ into a sulfur-deficient compound, with only Ni_3S_2 as detected subproduct. It has to be noted that the solvothermal reaction proceeded cleanly without precipitation of ferromagnetic Ni^0 metal (See discussion on magnetism in section 3.4), and it leaves only PPh_3 species in the residual solution (Fig. S1) besides gaseous CO. The similar results were obtained when the amount of $Ni(PPh_3)_2(CO)_2$ was reduced to 1.2 or 1.5 equiv. (Fig. S2). In all cases, the SEM/EDX analyses evidenced the absence of phosphorus element in the final product). Apart from the presence of different secondary phases, the overall XRD pattern was similar with the one obtained from the reaction with 0.5 equiv. of Ni^0 powder (Fig. 2a). However, its peak positions were significantly shifted to higher angle, making the pattern resemble the XRD pattern of *oA*-La_2O_2S (Fig. 2c). In fact,

Rietveld refinement using the *oA*-La_2O_2S model well explained the XRD pattern from the reaction with $Ni(PPh_3)_2(CO)_2$ with cell parameters a = 4.155 Å, b = 3.990 Å, c = 12.73 Å (V = 211.0 Å^3, see Fig. S4 and Table S1) slightly larger than the reported value[24] a = 4.149 Å, b = 3.975 Å, c = 12.73 Å (V = 209.9 Å^3). To estimate the possible sulfur off-stoichiometry, Rietveld refinement was carried out using an "hybrid" model where an additional sulfur site was placed just at the barycenter of the sulfur dimer in the *oA*-$La_2O_2S_{1.5}$ structure type (Fig. 3). In this model, occupancy of this additional sulfur site (Occ.(S3)) was constrained by that of sulfur dimers (Occ.(S1)) so that Occ.(S3) = 1- Occ.(S1) while the occupancy of the site normally occupied by S^{2-} anions (site S2) in *oA*-$La_2O_2S_{1.5}$ were fixed to 1. Accordingly, the hybrid model becomes similar to *oA*-La_2O_2S at Occ.(S1) → 0 limit, and *oA*-$La_2O_2S_{1.5}$ at Occ.(S1) → 1 limit, respectively. The refinement gave Occ.(S1) = 0.24(1) and Occ.(S3) = 0.76(1), corresponding the average composition $La_2O_2S_{1.12(1)}$ (See Table S1 for details). This off-stoichiometry can be understood by a disordered structure where $(S_2)^{2-}$ pairs may randomly alternate with S^{2-} species or where $La_4O_4S_3$ and La_2O_2S blocks may alternate, the latter being in the majority. This deintercalation of sulfur anions accompanied the formation of Ni_3S_2 Heazelwoodite[36] suggesting the reaction:

$$La_2O_2S_2 + 1.32\ Ni^0 \rightarrow La_2O_2S_{1.12} + 0.44\ Ni_3S_2$$

However, this hypothetical formula contradicted our SEM/EDX results that the solvothermal reaction introduced only 1.0 equiv. of Ni into the reaction mixture (Fig. S3). In addition, the hypothetical content of Ni_3S_2 (i.e. 44 mol% of the oxysulfide phase) far exceeded the molar ratio $La_2O_2S_{1.12}/Ni_3S_2$ = 1.000(2)/0.298(3) estimated from the refinement (Table S1). Those inconsistencies imply that the sulfur deintercalation does not represent the overall process of the solvothermal reactions. Some possible rationales are: (i) sulfur-rich Ni_xS_y were formed as amorphous phases or (ii) intercalation of Ni actually took also place forming $La_2O_2Ni_xS_2$ ($x \leq 1$) slabs, which were however too poorly crystalline or present too sparsely to be spotted on the diffraction pattern.

To better understand those poorly diffracting parts of the reaction mixture, we carried out investigations at the nanometric scale by transmission electron microscopy (TEM). Fig. 4a shows high-angle annular dark field (HAADF) scanning transmission electron microscope (STEM) images of the samples obtained after the solvothermal reaction of $La_2O_2S_2$ with Ni^0 complexes. This atomic-resolution image featured lamellar patterns consisting of zigzag-shaped bright strips. As we have previously reported[24], those bright strips correspond to the PbO-type $[La_2O_2]^{2+}$ slabs stacking in the sequence in *oA*-$La_2O_2S_{1.5}$ and *oA*-La_2O_2S (Fig. 2b-c).

EDX mapping overlaid on this HAADF-STEM image (Fig. 4b) indicated that some parts of grains were subject to 2D diffusion of Ni specie, resulting in irregular stacking of $[La_2O_2]^{2+}$ slabs. Other Ni-poor parts has the regular stacking of $[La_2O_2]^{2+}$ slabs with interlayer spacing around 6.4 Å (Fig. 4c), falling into the typical values of *oA*-$La_2O_2S_{1.5}$ (6.43 Å), *oA*-La_2O_2S (6.36 Å), and the refined *oA*-$La_2O_2S_{1.5-x}$ (6.36 Å for x ~ 0.38, see Table S1). La/S molar ratio of this Ni-poor domain was estimated by EDX and agreed with the presence of the sulfur-deintercalated $La_2O_2S_{1.5}$ phase.

The thickness of the Ni-rich domain, i.e. the distance between the two $[La_2O_2]^{2+}$ strips around the domain, was estimated from the HAADF-STEM intensity integrated on a large domain (white broken line rectangle) at around 19.8 Å (Fig. 4c). However a closer look on the TEM image revealed two important features of the Ni-intercalated domains. First the thickness of the Ni-rich region on a well-organized part is slightly smaller *i.e.* around 16.4 Å (See magnified image Fig. 4e). Second, another zigzag $[La_2O_2]^{2+}$ strip was present within this Ni-rich domain, though its scattering intensity was much weaker.

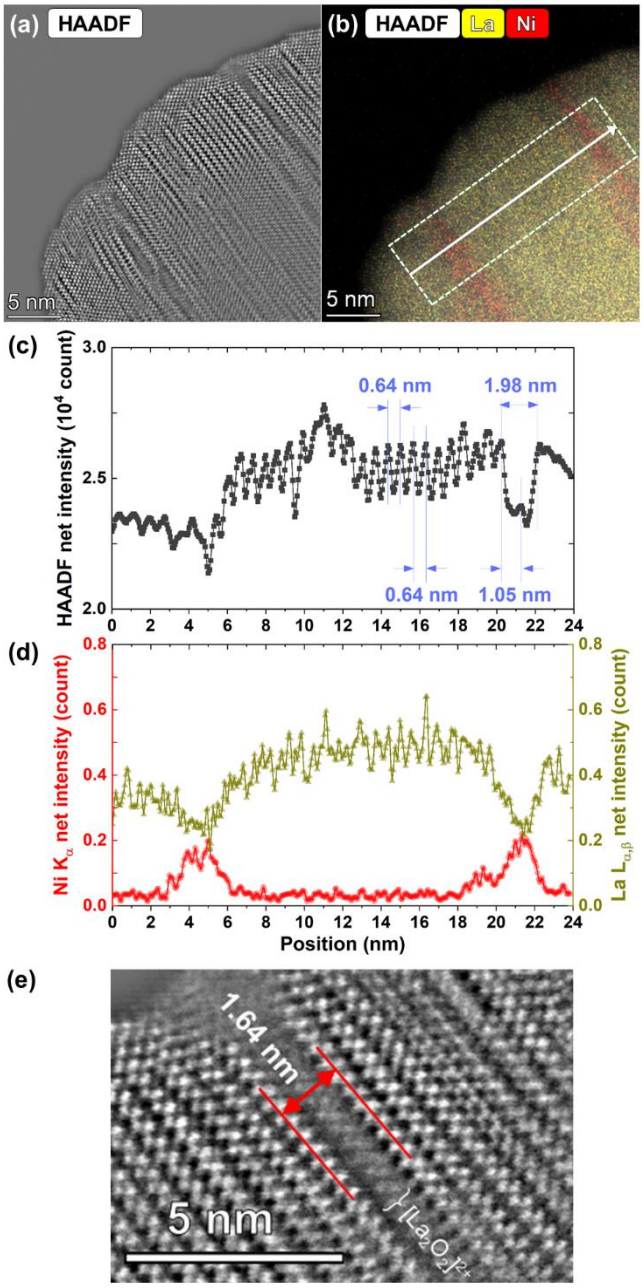

Fig. 4. (a) HAADF-STEM image and (b) EDX mapping of the selected grain obtained from the solvothermal reaction of $La_2O_2S_2$ with 2.0 equiv. of $Ni(PPh_3)_2(CO)_2$. The white broken line defines the domain in which HAADF-STEM and EDX signals were respectively integrated. The integrated intensities were then mapped along the white arrow in (c-d) the 1D plots. (e) Zoom-in view of the Ni-rich domain of the HAADF-STEM image in Fig. 4a.

Taking into account this another $[La_2O_2]^{2+}$ layer, makes the interlayer spacing between two consecutive $[La_2O_2]^{2+}$ slabs around 8.2 Å. This value is intermediate between the spacing observed in *oA*-La_2O_2S (6.36 Å), or $La_2O_2S_2$ precursor (6.61 Å)[37], and the known metal-intercalated analogs $La_2O_2Cu_2S_2$ (8.52 Å)[38].

Although it is too early to conclude anything about structures from this single feature, those values may be considered as the interlayer spacing of the unprecedented La-O-Ni-S phase, whose hypothetical structures are discussed later in the Section 3.4 with the computational structure prediction. In this case, the weaker scattering intensity of the Ni-rich domain (Fig. 4e) can be explained by its disordered structure arising from e.g. in-plane Ni heterogeneity. Another

possibility is that intercalation of Ni led to the nucleation of 2D Ni-S phase in between $[La_2O_2]^{2+}$ slabs. Our EDX mapping indicated the anti-correlation between the presence of Ni and La element (Fig. 4d; Note that the plot showed net intensities coming from respective elements, rather than atomic molar ratio). This implies that 2D diffusion of Ni accompanied disappearance of $[La_2O_2]^{2+}$ slabs, resulting in the biphasic composite where the *oA*-$La_2O_2S_{1.5-x}$ domains are intergrown with a 2D Ni-S phase. This partial removal of $[La_2O_2]^{2+}$ slabs also explains the weak scattering intensity of the Ni-rich domain in Fig. 4e.

The HAADF-STEM image in Fig 4a displayed very sparse presence of Ni-intercalated layers and numerous defects around them. Some other grains contained more Ni (See e.g. Fig S5). However, the higher contents of Ni intercalants not only further deteriorate crystallinity but also induce extreme beam sensitivity, which hampered us from obtaining any structural information from these Ni-rich grains neither by direct imaging nor by diffraction. That poor crystallinity of Ni-rich domains might explain why the XRD pattern in Fig. 2c did not provide any direct information about their Ni-intercalated layers.

3.2. Reactivity of $La_2O_2S_2$ towards Fe^0 and Co^0 metals

The similar observation was obtained when $La_2O_2S_2$ was treated with Fe^0 and Co^0 metals. As evidenced by the XRD patterns in Fig.5a, the $La_2O_2S_2$ precursor readily reacted with Fe^0 and Co^0 powders even by the solid-solid processes in the sealed silica tubes. The obtained reaction mixtures commonly exhibited the broad XRD patterns similar with the one obtained from the solvothermal reaction with the Ni^0 complex. This suggested the formation of the sulfur deintercalated *oA*-$La_2O_2S_{1.5-x}$ phases, but their peaks slightly shifted towards lower 2θ values in Fe and Co cases. Rietveld refinement using the *oA*-$La_2O_2S_{1.5-x}$ based hybrid model (Fig. 3a-b) confirmed that the reaction with Co^0 and Fe^0 powders actually led to the stoichiometric *oA*-$La_2O_2S_{1.5}$ phase (Occ.(S1) = 1.00(5) and Occ.(S1) = 1.00(2), respectively) with similar cell volumes of 438.8(2) Å^3 to compare with the expected value[24] of 439.1(1) Å^3 (See Fig. S6a and 6b, and Table S2 for details). However, Rietveld fit exhibited significant discrepancies in intensity at some peaks (Fig. S6b) for Fe, which was reflected in a poor goodness of fitting (GOF) of 3.09. Moreover the Fourier difference map calculated from this Rietveld refinement displayed some pronounced nuclear residues within sulfide layers and $[La_2O_2]^{2+}$ slabs (Fig. S7). The layered nature of the material suggests that this could be due to different types of stacks coexisting with $[La_2O_2]^{2+}[S_{1.5}]^{2-}$ domains.

The nature of such stacking disorder was studied by microscopic analyses. Fig. 5b displays the HAADF-STEM image and corresponding EDX mappings of the powder sample obtained from the reaction of $La_2O_2S_2$ with Fe^0 powder. In a similar way as the case of Ni, this oxysulfide grain consists of the bright and thick strips alternating regularly with darker and thinner strips. Although its poor crystallinity and beam sensitivity hampered acquisition of atomic-resolution image, the distance between two bright strips could be estimated at around 6.9 Å (Fig. S8), a value comparable with the interlayer spacing between $[La_2O_2]^{2+}$ slabs in $La_2O_2S_{2-x}$ series (6.4-6.6 Å, depending on $0 \leq x \leq 1.0$)[24]. In addition to these regular stacks, there were also thicker but dark strips, in which the EDX mapping indicated the systematic presence of Fe element. It evidenced that the solid-solid reaction triggered 2D diffusion of Fe intercalants in between some $[La_2O_2]^{2+}$ layers to give a possible La-O-Fe-S quaternary phase. The distance between the bright strips on either side of this thick dark ones was estimated at around 10.0-10.3 Å (Fig. S8). In contrast to structural diversity of its selenide counterparts[39-40], the La-O-Fe-S quaternary phase system is scarcely known, and $La_2O_2Fe_2OS_2$ is the sole example reported so far[41]. This compound also consists of PbO-type $[La_2O_2]^{2+}$ slabs alternating with $[Fe_2OS_2]^{2-}$ blocks with the interlayer spacing around 8.9 Å[42], which was significantly smaller than the value determined here within the Fe-intercalated domains in Fig. 5b. This discrepancy suggested that the intercalation of Fe metals brought about a new La-O-Fe-S quaternary phase. This should be confirmed by further investigations on materials with a higher degree of purity.

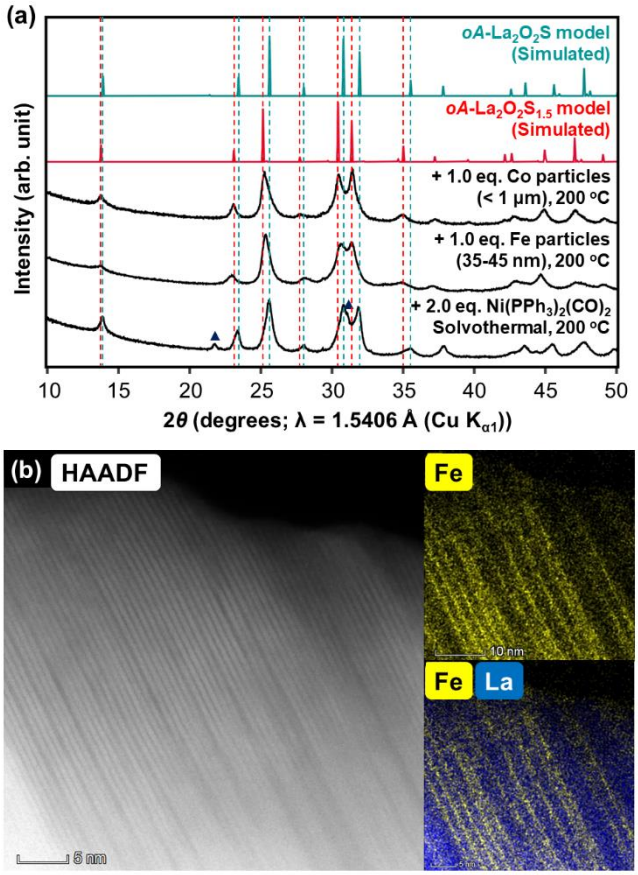

Fig. 5. (a) The experimental XRD (black) of the powder samples obtained from the reactions of $La_2O_2S_2$ with the respective transition metal species. The XRD patterns simulated for *oA*-$La_2O_2S_{1.5}$ and *oA*-La_2O_2S were also shown in red and cyan for comparison. The symbols represent diffraction peaks from ▲ = Ni_3S_2. (b) HAADF-STEM image and EDX mapping of the selected grain obtained from the solid-solid reaction of $La_2O_2S_2$ with 1.0 equiv. of Fe^0 powder

3.3. Structure prediction of possible $La_2O_2Ni_xS_y$ phases

Despite elusive characterization of intercalated species, it was at least evidenced by TEM that transition metals (i.e. Ni and Fe) intercalated into $La_2O_2S_2$ to construct metal sulfide layers. Therefore, it is worthwhile to discuss the possible structures of these intercalated layers, which mark the first example of lamellar La-O-Ni-S quaternary phase. We carried out a computational structure prediction on three hypothetical Ni-intercalated phases using the evolutionary algorithm USPEX[27] to get some insights on reactivity of Ni towards $La_2O_2S_2$ (See 2.1. Experimental procedures or details). The three compositions are (i) $La_2O_2NiS_2$ (the bulk composition suggested by SEM/EDX analysis (See Fig. S3)), (ii) $La_2O_2Ni_{0.5}S_2$ (case with less Ni than the bulk composition), and (iii) $La_2O_2Ni_{0.5}S_{1.5}$ (concomitant insertion of Ni with partial sulfur removal). 1539-4775 structures were generated over 32-80 generations and subject

to geometry optimizations implemented in VASP code using dispersion-corrected DFT-D3 method with Becke-Johnson (BJ) damping[28-29] (See the experimental procedure for the details). The lowest energy structures, their structural parameters, and the relative energies are summarized in Fig. S9-S11 and Table S3-S5.

Fig. 6 highlights the lowest-energy structure(s) predicted for $La_2O_2NiS_2$ and $La_2O_2Ni_{0.5}S_2$ compositions. For $La_2O_2NiS_2$, the predicted structure would adopt the lamellar architecture built on PbO-type $[La_2O_2]^{2+}$ slabs alternating with infinite-layer $[NiS_2]^{2-}$ slabs (Fig. 6a). These infinite $[NiS_2]^{2-}$ layers would consist of NiS_4 tetrahedra sharing corner (Fig. 6b), and two successive NiS_2 layers being shifted by a 0.5*a* + 0.5*b* vector (Fig. 6c). This structure type turns to be isostructural with the one of $La_2O_2CdSe_2$[43]. In addition to this $La_2O_2CdSe_2$ structure type, USPEX code predicted another similar structure within narrow enthalpy difference (Fig. S9). The only difference resided in the absence of 0.5*a* + 0.5*b* translation from one $[NiS_2]^{2-}$ slab to another. The remarkable point of those predicted structures are their flattened NiS_4 tetrahedra: S-Ni-S angle of the predicted structure (Fig. 6a) was 130.9°, being much larger than the ideal tetrahedron (109.5°), S-Cd-S in $La_2O_2CdSe_2$ (S-Cd-S angle of 99.8°) and S-Cu-S in $La_2O_2Cu_2S_2$ (S-Cu-S angle of 111.1°)[38]. In general, divalent cations of the group 10 elements (Ni^{2+}, Pd^{2+}, Pt^{2+}) tend to adopt such flattened geometries due to their d^8 electron configuration, as exemplified by square-planar coordination in $PdCh_2$ (Ch = S, Se)[44] and PtS[45]. Compared to Pd and Pt, the less diffused d-orbitals of Ni^{2+} (i.e. less susceptible to ligand fields and severer on-site coulomb repulsion) are not necessarily stabilized the most in the low-spin square planar configuration and Ni(II) compounds are often found with tetrahedral or octahedral coordination. Nevertheless, there are still number of Ni(II) compounds taking flattened geometries, such as square-pyramidal coordination in $BaNiS_2$[46] and square-planar cyanonickelate in $K_2Ni(CN)_4$[47]. In the current case, the weak ligand field of S^{2-} anions was likely to favor a tetrahedral coordination but with a flattened geometry.

The lowest-energy structure using the same approach for the $La_2O_2Ni_{0.5}S_2$ composition was built upon PbO-type $[La_2O_2]^{2+}$ slabs and $[NiS_2]^{2-}$ slabs with the S-Ni-S angles around 130° (Fig. 6d). Since only 0.5 equiv. of Ni was introduced into the system, only one sulfide layer over two of the $La_2O_2S_2$ precursor was intercalated (Fig. 6e-f). This structure can be regarded as a composite with many intergrowths between reduced $La_2O_2S_2$ domains (mainly built on oA-$La_2O_2S_{1.5-x}$ variants) and Ni intercalated $La_2O_2S_2$ domains. Another remarkable feature of this structure is the stripe-like ordering of its edge-sharing NiS_4 tetrahedra. This stripe-like ordering of metal sulfide was also found in its structural analogs *oI*-$La_2O_2FeSe_2$[39] but this ordering gradually changes into checkerboard-like ordering depending on metal species and its ratio[48]. This implies that various types of ordering may be possible with small energy costs also in the case of this predicted structure.

The lowest-energy structure(s) predicted for $La_2O_2NiS_2$ and $La_2O_2Ni_{0.5}S_2$ compositions (Fig. 6) shows an alternation of on PbO-type $[La_2O_2]^{2+}$ slabs and infinite-layer $[NiS_2]^{2-}$. In both cases the interlayer spacing between two consecutive $[La_2O_2]^{2+}$ layers sandwiching the $[NiS_2]^{2-}$ layer are in the range 7.4-7.6 Å (Fig. 6). These predicted values are not far from the experimental one (8.2 Å) as extracted from the TEM image (Fig. 4e). It suggests that the Nickel sulfide layer formed in between the $[La_2O_2]^{2+}$ slabs may contain corner or edge sharing NiS_4 tetrahedra.

Finally, the lowest-energy structure predicted for $La_2O_2Ni_{0.5}S_{1.5}$ was more eccentric (Fig. S10) and for this reason was rebutted. Its nickel sulfide layers exhibited both monoatomic S^{2-} anions and $[S_2]^{2-}$ dimers as seen also in *oA*-$La_2O_2S_{1.5}$ (Fig. 2a) suggesting the presence of Ni^0. Nickel cation was connected to both sulfur species to form a 1D chain. In addition, stacking sequence of $[La_2O_2]^{2+}$ slabs remained in the one found from $La_2O_2S_2$ precursor (Fig. 1). The structure seems less likely, especially given the strange coordination environments of Ni cations bonded with sulfur dimers.

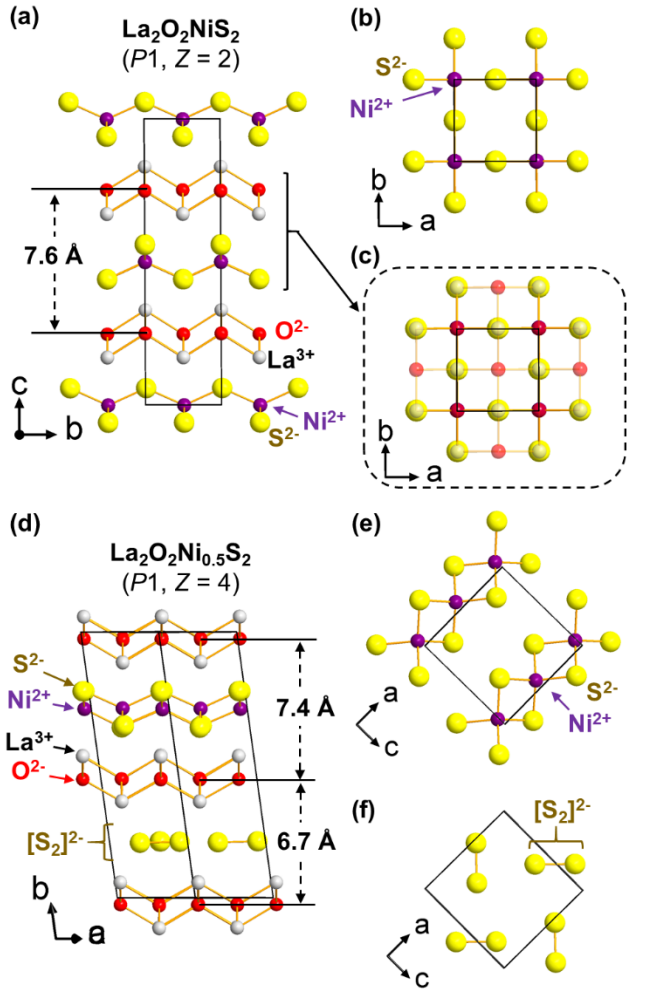

Fig. 6. Possible structures of La-O-Ni-S quaternary phases predicted computationally using USPEX algorithm. Each panel shows the lowest-energy structure predicted for respective compositions of (a-c) $La_2O_2NiS_2$ and (d-e) $La_2O_2Ni_{0.5}S_2$. See Fig. S9-S11 and Table S3-S5 for details.

3.4. Physical Characterization of Metal intercalants

For better understanding of intercalated metal species, magnetometry analyses were attempted for the samples prepared by the reaction of $La_2O_2S_2$ with 1.0 equiv. of Fe or Co nanoparticles, or with $Ni(PPh_3)_2(CO)_2$ (1:2 ratio). In the case of Co and Fe products the samples were contaminated by large amount of residual Fe or Co nanoparticles and or other paramagnetic phases which hindered drawing reliable conclusions from the data. Conversely, the contamination was much smaller in case of Ni intercalants which enabled the data treatment. Fig. 7a-b display the magnetization vs. field and susceptibility vs. temperature magnetic characteristics the samples prepared from $La_2O_2S_2$ and $Ni(PPh_3)_2(CO)_2$ (1:2 ratio). Its mass magnetization M_{mass} exhibited linear dependence on applied field at 100 K $\leq T \leq$ 300 K, and as temperature decreased, it gradually started following a Brillouin function behaving like $dM/dH \rightarrow 0$ at $H/T \rightarrow \infty$ limit. Accordingly, linear fits of *M* vs. *T* gave very small y-intercepts that were constant around $6.6(3) \times 10^{-5}$ emu (Fig. S12). That subtle ferromagnetic signal can be attributed to the presence of undetected traces of Ni^0 metal, which exhibited saturated magnetization ($M_{sat,max}$ = 58.57 emu g^{-1}) already around 300 K[49].

Indeed, Ni content estimated by dividing y-intercept by $M_{sat,max}$ accounted for only 11 ppm of the sample. Such a small Ni content showcases the excellent performance of thermally stable $Ni(CO)_2(PPh_3)_2$ complexes as a Ni^0 source that selectively reacts with the oxysulfide avoiding precipitation of Ni^0 nanoparticles.

Molar susceptibility χ_{mol} of that specimen was calculated after subtracting the ferromagnetic signal from Ni^0 as well as diamagnetic signals from plastic sample holder (See the experimental section for the details). Formula unit of the overall mixture was supposed to be $La_2O_2NiS_2$ (Fw = 432.62 g mol^{-1}), following its SEM/EDX data. Fig. 7b plots the obtained χ_{mol} against temperature. Its temperature dependence seems to be a typical paramagnet following Curie-Weiss law:

$$\chi_{mol} = C / (T - \Theta)$$

,where C and Θ denote Curie constant and Weiss constant, respectively. However, there was also a significant contribution from a temperature-independent term as evidenced by linear slope on the plot of $\chi_{mol}T$ against temperature. That additional component could be rationalized by the presence of the Ni_3S_2 by-product detected by XRD (Fig. 2d), which is known to be a Pauli paramagnetic metal with χ_{mol} around 7.2×10^{-5} emu mol^{-1} Oe^{-1}.[50] Accordingly, χ_{mol} was fitted taking also the temperature-independent term α into account:

$$\chi_{mol} = C / (T - \Theta) + \alpha$$

Fitting within the temperature range of 100 K ≤ T ≤ 300 K gave C = $7.8(7) \times 10^{-3}$ emu K mol^{-1} Oe^{-1}, Θ = 19(6) K and α = $5.8(2) \times 10^{-5}$ emu mol^{-1} Oe^{-1} (Fig. S13). The striking fact is that effective moment estimated from Curie constant amounted only to $\mu_{eff} \approx \sqrt{8C}$ = 0.25(1) μ_B, which was far smaller than the spin-only μ_{eff} of Ni^{2+} (d^8, 2.83 μ_B), and even of Ni^+ (d^9, 1.73 μ_B). Such a small effective moment suggested that almost all Ni cations in the reaction mixture delocalize their valence electrons through metallic bonds.

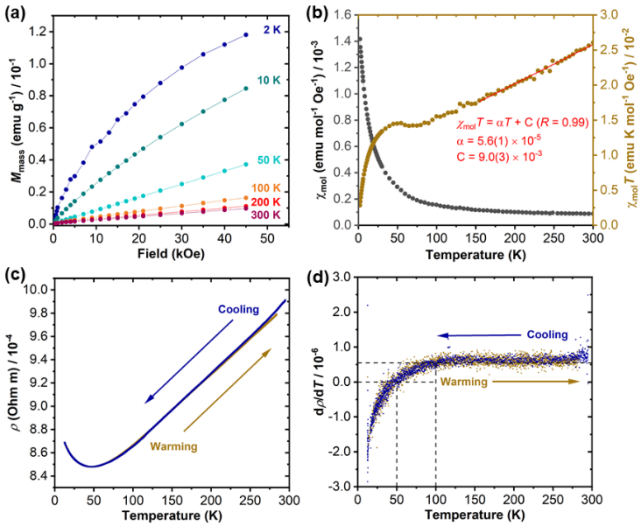

Fig. 7. Magnetic and electric transport properties of the sample after the reaction of $La_2O_2S_2$ with Ni^0 complexes under solvothermal condition. (a) Mass magnetisation M_{mass} plotted against applied field. (b) Molar susceptibility χ_{mol} and its product with temperature $\chi_{mol}T$ plotted against temperature T. Applied field: 30 kOe. χ_{mol} was calculated supposing average composition estimated by SEM/EDX: $La_2O_2NiS_2$ (Fw = 432.62 g mol^{-1}). Linear fitting (red line) was performed for $\chi_{mol}T$ in temperature range of 100 K ≤ T ≤ 300 K. (c) Electric resistivity ρ and (d) its derivative $d\rho/dT$ plotted against temperature. Data acquired during cooling and warming processes are plotted in navy and yellow, respectively. The powder sample was pelletized and annealed at 200 °C in acetonitrile before the transport measurement.

This observation was supported also by electric transport measurements (Fig. 7c-d). The final product of the $La_2O_2S_2$ - $Ni(PPh_3)_2(CO)_2$ mixture exhibited a metallic behavior with a linear increase of resistivity ρ with temperature. One of the rationales for this metallic behavior is deintercalation of sulfur from $La_2O_2S_2$ giving Pauli paramagnet metal Ni_3S_2 on the surface of the oxysulfide grains, which might create percolation pathways for electric transports. On the other hand, the resistance versus temperature curve of the mixture shows an upturn at around 50 K which is accompanied in the similar temperature range by a deviation of χ_{mol} from Curie-Weiss law (Fig. 5b). Neither the upturn observed in the electric measurement nor the magnetic anomaly can be explained by Ni_3S_2 or other known compounds in the binary Ni-S systems [50-51]. As the product is not completely pure it is not possible to draw a definitive conclusion regarding the physical behavior of Ni species intercalated into $La_2O_2S_x$ oxysulfides. However our measurements advocates more in favor of a charge delocalization (metallic like behavior) than a charge localization in these intercalated species.

4. Conclusion

The mixed anion compound $La_2O_2S_2$ containing $[S_2]^{2-}$ dimers may react with metal species in two different manners. The reaction leads either to the topochemical intercalation of the metal in the case of Cu, [19] or to the topochemical deinterclation of half of the sulfur atoms of the dimer in the case of Rb. [24] In this study we explore further the reactivity of the mixed anion compound $La_2O_2S_2$ with transition metals Fe, Co and Ni. We found that the reaction with these transition metals leads to a competition between both processes at the local scale. Our X-ray diffraction analyses of the bulk revealed that the reaction with those transition metals conducts to the partial de-intercalation of sulfur species from $La_2O_2S_2$, leading to the formation of $La_2O_2S_{1.5-x}$ ($0 \le x \le 0.38$) products. But in the meantime our nanoscale observations by scanning transmission electron microscopy (STEM) clearly evidenced that Ni and Fe cations diffused in between $[La_2O_2]^{2+}$ slabs to interact with $[S_2]$ species, forming at the end a composite material built on the intergrowth of $La_2O_2S_{1.5-x}$ ($0 \le x \le 0.38$) blocks and $La_2O_2M_yS_{2-x}$ blocks. Preliminary structure prediction calculations suggest that in case of Ni the transition metal layer may be built with edge sharing or corner sharing NiS_4 tetrahedra. This finding suggest therefore the formation of nickel and iron sulfide layers either in an unprecedented La-O-M-S (M = Ni, Fe) phase, or a biphasic heterostructure.

AUTHOR INFORMATION

Corresponding Author

Shunsuke.saski@cnrs-imn.fr; Stephane.jobic@cnrs-imn.fr; Laurent.cario@cnrs-imn.fr

REFERENCES

1. Whittingham, M. S. Electrical Energy Storage and Intercalation Chemistry. *Science*, 1976, **192**, 1126-1127.
2. Whittingham, M. S. Chemistry of intercalation compounds: Metal guests in chalcogenide hosts. *Prog. Solid St. Chem.* **1978**, *12*, 41-99.
3. Guillamón, I.; Suderow, H.; Vieira, S.; Cario, L.; Diener, P.; Rodière, P. Superconducting Density of States and Vortex Cores of 2H-NbS_2. *Phys. Rev. Lett.* **2008**, *101*, 166407.
4. Fang, Y. Q.; Pan, J.; He, J. Q.; Luo, R. C.; Wang, D.; Che, X. L.; Bu, K. J.; Zhao, W.; Liu, P.; Mu, G.; Zhang, H.; Lin, T. Q.; Huang, F. Q. Structure Re-determination and Superconductivity Observation of Bulk 1T-MoS_2. *Angew. Chem., Int. Ed.* **2018**, *57*, 1232-1235.
5. Wilson, J. A.; Di Salvo, F. J.; Mahajan, S. Charge density waves in metallic, layered, transition-metal dichalcogenides. *Phys. Rev. Lett.* **1974**, *37*, 882.
6. Ma, L.; Ye, C.; Yu, Y.; Lu, X. F.; Kim, S.; Feng, D.; Tománek, D.; Son, Y.-W.; Chen, X. H.; Zhang, Y. A metallic mosaic phase and the

origin of Mott-insulating state in 1T-TaS_2. *Nat. Commun.* **2016**, *7*, 10956.
7. Leriche, R.; Morales, A. P.; Campetella, M.; Tresca, C.; Sasaki, S.; Brun, C.; Debontridder, F.; David, P.; Arfaoui, I.; Šofranko, O.; Samuely, T.; Kremer, G.; Monney, C.; Jaouen, T.; Cario, L.; Calandra, M.; Cren, T. Misfit Layer Compounds: A Platform for Heavily Doped 2D Transition Metal Dichalcogenides. *Adv. Funct. Mater.* **2020**, *31*, 2007706.
8. Qian, X.; Liu, J.; Fu, L.; Li, J. Quantum spin Hall effect in two-dimensional transition metal dichalcogenides. *Science* **2014**, *346*, 1344-1347.
9. Voiry, D.; Yang, J.; Chhowalla, M. Recent Strategies for Improving the Catalytic Activity of 2D TMD Nanosheets Toward the Hydrogen Evolution Reaction. *Adv. Mater.* **2016**, *28*, 6197-6206.
10. Huh, W.; Lee, D.; Lee, C.-H. Memristors Based on 2D Materials as an Artificial Synapse for Neuromorphic Electronics. *Adv. Mater.* **2020**, *32*, 2002092
11. Hu, C.; Ding, L.; Gordon, K. N.; Ghosh, B.; Tien, H.-J.; Li, H.; Linn, A. G.; Lien, S.-W.; Huang, C.-Y.; Mackey, S.; Liu, J.; Reddy, P. V. S.; Singh, B.; Agarwal, A.; Bansil, A.; Song, M.; Li, D.; Xu, S.-Y.; Lin, H.; Cao, H.; Chang, T.-R.; Dessau, D.; Ni, N. Realization of an intrinsic ferromagnetic topological state in $MnBi_8Te_{13}$. *Sci. Adv.* **2020**, *6*, eaba4275.
12. Shibauchi, T.; Hanaguri, T.; Matsuda, Y. Exotic Superconducting States in FeSe-based Materials. *J. Phys. Soc. Jpn.* **2020**, *89*, 102002.
13. Murphy, D. W.; Cros, C.; Di Salvo, F. J.; Waszczak, J. V. Preparation and Properties of Li_xVS_2 ($0 < x < 1$). *Inorg. Chem.* **1997**, *16*, 3027-3031.
14. Van Bruggen, C. F.; Haange, R. J.; Wiegers, G. A.; De Boer, D. K. G. $CrSe_2$, A New Layered Dichalcogenide. *Physica* **1980**, *99B*, 166-172.
15. Lin, H.; Si, J.; Zhu, X.; Cai, K.; Li, H.; Kong, L.; Yu, X.; Wen, H.-H. Structure and physical properties of $CsV_2Se_{2-x}O$ and V_2Se_2O. *Phys. Rev. B* **2018**, *98*, 075132
16. Ablimit, A.; Sun, Y.-L.; Cheng, E.-J.; Liu, Y.-B.; Wu, S.-Q.; Jiang, H.; Ren, Z.; Li, S.; Cao, G.-H. V_2Te_2O: A Two-Dimensional van der Waals Correlated Metal. *Inorg. Chem.* **2018**, *57*, 14617–14623
17. Borg, C. K. H.; Zhou, X.; Eckberg, C.; Campbell, D. J.; Saha, S. R.; Paglione, J.; Rodriguez, E. E. Strong anisotropy in nearly ideal tetrahedral superconducting FeS single crystals. *Phys. Rev. B* **2016**, 93, 094522.
18. Zhou, X.; Wilfong, B.; Vivanco, H.; Paglione, J.; Brown, C. M.; Rodriguez, E. E. Metastable layered cobalt chalcogenides from topochemical deintercalation. *J. Am. Chem. Soc.* **2016**, *138*, 16432−16442.
19. Sasaki, S.; Driss, D.; Grange, E.; Mevellec, J.-Y.; Caldes, M. T.; Guillot-Deudon, C.; Cadars, S.; Corraze, B.; Janod, E.; Jobic, S.; Cario, L. A Topochemical Approach to Synthesize Layered Materials Based on the Redox Reactivity of Anionic Chalcogen Dimers. *Angew. Chem., Int. Ed.* **2018**, *57*, 13618−13623.
20. Sasaki, S.; Steciuk, G.; Guillot-Deudon, C.; Caldes, M. T.; Braems, I.; Janod, E.; Corraze, B.; Jobic, S.; Cario, L. Solvothermal and mechanochemical intercalation of Cu into $La_2O_2S_2$ enabled by the redox reactivity of $(S_2)^{2-}$ pairs. *Dalton Trans.* **2021**, *50*, 12419-12423.
21. Sasaki, S.; Giri, S.; Cassidy, S.J.; Dey, S.; Batuk, M.; Vandemeulebroucke, D.; Cibin, G.; Smith, R. I.; Holdship, P.; Grey, C. P.; Hadermann, J.; Clarke, S. J. Anion redox as a means to derive layered manganese oxychalcogenides with exotic intergrowth structures. *Nat. Commun.* **2023**, *14*, 2917.
22. Chaupatnaik, A.; Abakumov, A. M.; Rousse, G.; Foix, D.; Louis, J; Leube, B. T.; Tarascon, J.-M. Electrochemical Exploration of Layered Cu-Based Oxychalcogenides Obtained Topochemically via Anionic Redox and Displacement Reaction. *Chem. Mater.* **2023**, *35*, 5924-5935.
23. Sasaki, S.; Lesault, M.; Grange, E.; Janod, E.; Corraze, B.; Cadars, S.; Caldes, M. T.; Guillot-Deudon, C.; Jobic, S.; Cario, L. Unexplored reactivity of $(S_n)^{2-}$ oligomers with transition metals in low-temperature solid-state reactions. *Chem. Commun.* **2019**, *55*, 6189-6192.
24. Sasaki, S.; Caldes, M. T.; Guillot-Deudon, C.; Braems, I.; Steciuk, G.; Palatinus, L.; Gautron, E.; Frapper, G.; Janod, E.; Corraze, B.; Jobic, S.; Cario, L. Design of Metastable Oxychalcogenide Phases by Topochemical (de)Intercalation of Sulfur in $La_2O_2S_2$. *Nat. Commun.* **2021**, *12*, 3605.
25. Zhao, Y.-W.; Zheng, R. K.; Zhang, X. X.; Xiao, J. Q. A simple method to prepare uniform Co nanoparticles. *IEEE Trans. Magn.* **2003**, *39*, 2764-2766.
26. Stephens, P. W. Phenomenological model of anisotropic peak broadening in powder diffraction. *J. Appl. Cryst.* **1999**, *32*, 281-289.
27. Oganov, A. R.; Lyakhov, A. O.; Valle, M. How evolutionary crystal structure prediction works –and why. *Acc. Chem. Res.* **2011**, *44*, 227–237.
28. Grimme, S.; Antony, J.; Ehrlich, S.; Krieg, H. A consistent and accurate ab initio parametrization of density functional dispersion correction (DFT-D) for the 94 elements H-Pu. *J. Chem. Phys.* **2010**, *132*, 154104.
29. Grimme, S.; Ehrlich, S.; Goerigk, L. Effect of the damping function in dispersion corrected density functional theory. *J. Comput. Chem.* **2011**, *32*, 1456-1465.
30. Trahan, J.; Goodrich, R. G.; Watkins, S. F. X-Ray Diffraction Measurements on Metallic and Semiconducting Hexagonal NiS. *Phys. Rev. B* **1970**, *2*, 2859.
31. Morosin, B. La_2O_2S structure refinement and crystal field. *Acta Cryst.* **1973**, *B29*, 2647-2648.
32. Koski, K. J.; Wessells, C. D.; Reed, B. W.; Cha, J. J.; Kong, D.; Cui, Y. Chemical Intercalation of Zerovalent Metals into 2D Layered Bi 2 Se 3 Nanoribbons. *J. Am. Chem. Soc.* **2012**, *134*, 13773–13779.
33. Wang, M.; Williams, D.; Lahti, G.; Teshima, S.; Dominguez Aguilar, D.; Perry, R.; Koski, K. J. Chemical Intercalation of Heavy Metal, Semimetal, and Semiconductor Atoms into 2D Layered Chalcogenides. *2D Mater.* **2018**, 5, 045005.
34. Shi, Z. Nickel carbonyl: toxicity and human health. *Sci. Total Environ.* **1994**, *148*, 293-298.
35. Colthup, E. C.; Meriwether, L. S. Polymerization of Acetylenes by Nickel-Carbonyl-Phosphine Complexes. III. Polymers from Terminal-Unconjugated Diacetylenes. *J. Org. Chem.* **1961**, *26*, 5169–5175.
36. Parise, J. B. Structure of hazelwoodite (Ni_3S_2). *Acta Cryst.* **1980**, *B36*, 1179-1180.
37. Ostoréro, J.; Leblanc, M. Room-temperature structure of $La_2O_2S_2$. *Acta Cryst.* **1990**, *C46*, 1376-1378.
38. Ueda, K., Takafuji, K. and H. Hosono, H. Preparation and crystal structure analysis of CeCuOS. *J. Solid State Chem.* **2003**, 170, 182-187.
39. Nitsche, F.; Niklaus, R.; Johrendt, D. New Polymorphs of $RE_2FeSe_2O_2$ (*RE* = La, Ce). *Z. Anorg. Allg. Chem.* **2014**, *640*, 2897– 2902.
40. McCabe, E. E.; Free, D. G.; Mendis, B. G.; Higgins, J. S.; Evans, J. S. O. Preparation, Characterization, and Structural Phase Transitions in a New Family of Semiconducting Transition Metal Oxychalcogenides β-$La_2O_2MSe_2$ (*M* = Mn, Fe). *Chem. Mater.* **2010**, *22*, 6171– 6182.
41. Mayer, J. M.; Schneemeyer, L. F.; Siegrist, T.; Waszczak, J. V.; Van Dover, B. New Layered Iron-Lanthanum-Oxide-Sulfide and -Selenide Phases: $Fe_2La_2O_3E_2$ (E = S,Se). *Angew. Chem., Int. Ed.* **1992**, *31*, 1645–1647.
42. Freelon, B.; Yamani, Z.; Swainson, I.; Flacau, R.; Karki, B.; Liu, Y. H.; Craco, L.; Laad, M.S.; Wang, M.; Chen, J.; Birgeneau, R. J.; Fang, M. Magnetic and structural properties of the iron oxychalcogenides $La_2O_2Fe_2OM_2$ (*M* = S,Se). *Phys. Rev. B* **2019**, *99*, 024109.
43. Hiramatsu, H.; Ueda, K.; Kamiya, T.; Ohta, H.; Hirano, M.; Hosono, H. Synthesis of single-phase layered oxychalcogenide $La_2CdO_2Se_2$: crystal structure, optical and electrical properties. *J. Mater. Chem.* **2004**, *14*, 2946– 2950.
44. Dai, D.; Koo, H.-J.; Whangbo, M.-H.; Soulard, C.; Rocquefelte, X.; Jobic, S. Trends in the structure and bonding in the layered platinum dioxide and dichalcogenides PtQ_2 (Q = O, S, Se, Te). *J. Solid State Chem* **2003**, *173*, 114.
45. Collins, R.; Kaner, R.; Russo, P.; Wold, A.; Avignant, D. High-pressure phase transformation of platinum sulfide. *Inorg. Chem.* **1979**, *18*, 727–729.
46. Grey, I. E.; Steinfink, H. Crystal structure and properties of barium nickel sulfide, a square-pyramidal nickel(II) compound. *J. Am. Chem. Soc.* **1970**, *92*, 5093–5095.
47. Vannerberg, N.G. The crystal structure of $K_2Ni(CN)_4$. *Acta Chem. Scand.* **1964**, *18*, 2385-2391.
48. Ainsworth, C. M.; Wang, C.-H.; Johnston, H. E.; McCabe, E. E.; Tucker, M. G.; Brand, H. E. A.; Evans; J. S. O. Infinitely Adaptive Transition-Metal Ordering in $Ln_2O_2MSe_2$-Type Oxychalcogenides. *Inorg. Chem.* **2015**, *54*, 7230–7238
49. Danan, H.; Herr, A.; Meyer, A. J. P. New Determinations of the Saturation Magnetization of Nickel and Iron. *J. Appl. Phys.* **1968**, *39*, 669-670.
50. Metcalf, P. A.; Crooker, B. C.; McElfresh, M.; Kąkol, Z.; Honig, J. M. Low-temperature electronic and magnetic properties of single-crystal Ni_3S_2. *Phys. Rev. B* **1994**, *50*, 2055.
51. Rao, C. N. R.; Pisharody, K. P. R. Transition metal sulfides. *Prog. Solid State Chem.* 1976, **10**, 207-270.

Graphical abstract